Geophysical Journal International

Geophys. J. Int. (2020) **222,** 461–473
Advance Access publication 2020 April 14
GJI Geodynamics and tectonics

doi: 10.1093/gji/ggaa178

Triggering relationships between magmatic and faulting processes in the May 2018 eruptive sequence at Kīlauea volcano, Hawaii

Bhaskar Kundu,[1] Rajeev Kumar Yadav,[2] Roland Bürgmann,[3] Kang Wang,[3] Dibyashakti Panda[1] and Vineet K. Gahalaut[4]

[1] *Department of Earth and Atmospheric Sciences, NIT Rourkela, Rourkela, Odisha-769008, India. E-mail: rilbhaskar@gmail.com*
[2] *Institute of Seismological Research, Gandhinagar, Gujarat-328009, India*
[3] *Department of Earth and Planetary Science and Berkeley Seismological Laboratory, University of California, Berkeley, CA ,* 97720-4767, USA
[4] *CSIR-National Geophysical Research Institute, Hyderabad,* Telangana-500007, *India*

Accepted 2020 April 9. Received 2020 March 28; in original form 2019 July 30

SUMMARY

The May 2018 activity at Kīlauea Volcano, Hawaii involved magma transport and dyke intrusion along the East Rift Zone (ERZ) and nucleation of the 4 May 2018 *M* 6.9 earthquake along the basal décollement of Kīlauea's mobile south flank. Combined Global Positioning Systems (GPS) and Interferometric Synthetic Aperture Radar (InSAR) measurements captured the deformation sequence associated with the dyke intrusion, main shock and eruption episode along the ERZ. The earthquake was encouraged by static stress changes from the preceding magma reservoir inflation, ERZ expansion and fault creep on the décollement downdip of the rupture. Slip models derived from the inversion of GPS displacements indicate peak coseismic slip of 2–3 m. Our model analyses, including of the pre-May 2018 deformation, suggest that prior to this event there was no slip on the section of the décollement that ruptured in the earthquake. The observed magma inflation, rapid fault creep on the décollement and coseismic rupture reflect complex cyclic interactions between the magmatic and faulting processes.

Key words: Earthquake dynamics; Volcano seismology; Oceanic hotspots and intraplate volcanism; Magma chamber processes.

1 INTRODUCTION

The father of evolution, Darwin (1840) was probably the first to take cognizance of a volcanic eruption in Chile following a strong earthquake in 1835. Since then, volcanic eruptions have often been found to be spatio-temporarily linked with the occurrence of large earthquakes (Hill *et al.* 2002; Selva *et al.* 2004; Walter *et al.* 2005; Manga & Brodsky 2006; Walter & Amelung 2006, 2007; Pritchard *et al.* 2013; Takada & Fukushima 2013). Abnormal ground subsidence along the volcanic arc was observed within weeks of the 2010 *M* 8.8 Maule earthquake, Chile (Pritchard *et al.* 2013), while both ground subsidence and enhanced seismicity was recorded during the 2011 *M*9.0 Tohoku-Oki earthquake, Japan due to stretching of the volcanic edifice in the overriding plate (Takada & Fukushima 2013). Hill *et al.* (2002) suggest that a large earthquake can trigger or increase volcanic activity by both dynamic and static deformation. Walter & Amelung (2006) argue that subduction megathrust earthquakes of $M > 9$ produce static volumetric expansion in the volcanic arc that can lead to volcanic eruptions. Dynamic shaking has been found to trigger volcanic activity over a wide range of distances and with variable temporal delays, suggesting changes in magma overpressure due to the growth and rise of bubbles or failure of rocks surrounding magma chambers (Manga & Brodsky 2006). Time-dependent relaxation processes, such as viscoelastic flow and the emission of gases may affect the effectiveness and introduce delays in both static and dynamic triggering mechanisms (Manga & Brodsky 2006).

In turn, it has also been suggested that the static stress changes caused by magmatic processes may change the local stress regime and can trigger (or even supress) earthquakes on nearby faults. For example, magma reservoir inflation and dyke intrusions at Mauna Loa volcano, Hawaii and associated rift zones, encourage earthquakes on a deep décollement underlying the south flank of the volcano (Walter & Amelung 2006; Amelung *et al.* 2007), while earthquakes were discouraged on the Kaoiki fault zone lying to the west of Kīlauea (Walter & Amelung 2006). Similar interactions have been recognized between intrusive activity along Kīlauea volcano's rift zones and small and large earthquakes on the 6–9 km deep décollement underlying its south flank (e.g. Ando 1979; Dieterich *et al.* 2000; Denlinger & Morgan 2014). Continuous seaward motion of Kīlauea's south flank can lead to large earthquakes and associated tsunamis as well as to dyke intrusions along its rift

zones (Denlinger & Morgan 2014; Poland *et al.* 2014), however the exact nature of interaction among all these processes remains elusive. Other basaltic volcanoes (e.g. Mount Etna, Italy, the Canary Islands and Piton de la Fournaise on Réunion Island) also demonstrate flank instability and interaction of the magmatic system with active faults, with evidence of magmatic intrusions and eruptions triggering fault slip and vice versa (e.g. Borgia *et al.* 2000; Walter *et al.* 2005; Poland *et al.* 2017).

At Kīlauea volcano, Hawaii, the complex volcano-tectonic interaction is characterized by (i) expansion of its two rift zones (i.e. the ERZ and Southwest Rift Zone), probably involving continuous slow intrusion of magma into the deep rift zones and rapid and episodic dyke injections into the shallow rift system that sometimes lead to eruptive fissures (Dvorak *et al.* 1986; Delaney *et al.* 1993; Dieterich *et al.* 2000; Owen *et al.* 2000a), (ii) earthquakes rupturing the décollement at the base of Kīlauea's mobile south flank (Ando 1979; Dieterich *et al.* 2000; Owen & Bürgmann 2006) and (iii) steady fault creep (Owen *et al.* 2000a) and slow slip events (SSEs) on the décollement (Brooks *et al.* 2006; Segall *et al.* 2006; Foster *et al.* 2013; Montgomery-Brown *et al.* 2015).

Kīlauea Volcano had been erupting from the Pu'u 'Ō'ō and Kūpaianaha vents on the ERZ almost continuously from 1983 until 2018 (Heliker & Mattox 2003). These vents are laterally connected with a magma storage reservoir beneath Kīlauea's summit caldera (Cervelli & Miklius 2003; Larson *et al.* 2010, Fig. 1). A new fissure erupted in Nāpau Crater on 30 January 1997 along the ERZ due to a small underlying dyke injection (Owen *et al.* 2000b). ERZ intrusions and eruptions uprift of Pu'u 'Ō'ō that were captured by continuous GPS and InSAR measurements also occurred in the Father's Day episode starting 17 June 2007 (e.g. Montgomery-Brown *et al.* 2010) and the Kamoamoa episode lasting from March to May of 2011 (Lundgren *et al.* 2013). These episodes were associated with rapid summit deflation and seismic swarms accompanying the dilation along the ERZ (Lundgren *et al.* 2013; Segall *et al.* 2013). It has been suggested that the SSEs on the décollement have the potential to trigger volcanic activity in the magma system and vice-a-versa (Montgomery-Brown *et al.* 2015).

Improved understanding of volcano-earthquake interaction processes is important both for seismic hazard assessment and for volcano risk mitigation. This motivates us to explore the recent May 2018 dyke intrusion along Kīlauea's East Rift Zone (ERZ) and associated faulting episode on the décollement underlying Kīlauea's mobile south flank on Hawaii Island (Fig. 1). Keeping that in mind, we have organized this contribution in the following way. After a brief introduction about volcano-earthquake interaction processes and flank instability, we provide a timeline of the eruptive sequence and seismic activity on Kīlauea's ERZ in Section 2. In Section 3, we specify the complete set of data (GPS and InSAR) and modelling approaches used to characterize the deformation associated with the 4 May 2018 *M*6.9 earthquake. In Section 4.1, we characterize the deformation due to the May 2018 dyke intrusion and décollement faulting episode by considering both GPS and InSAR observations. Next, we consider the long-term deformation prior to the May 2018 eruption-earthquake, relying on cGPS-derived velocities for the period of 2013–2018. In Section 4.3, we target the precursory deformation process leading up to the 4 May 2018, *M*6.9 earthquake by jointly inverting the GPS and InSAR observations between 04/20/2018 and 05/02/2018. Finally, we discuss the static stress changes associated with the earthquake-volcano interaction cycle during the 2018 eruption-earthquake sequence on Kīlauea's ERZ.

2 MAY 2018 DYKE INTRUSION AND FAULTING EPISODE ON KĪLAUEA'S EAST RIFT ZONE

In the months preceding the episode, deep long-period earthquake activity, seismic velocity changes and deformation measurements suggest accelerated magma supply to Kīlauea's magma storage system (Neal *et al.* 2018; Olivier *et al.* 2019). Intrusive activity directly associated with the 2018 eruptive sequence at Kīlauea volcano on Hawaii initiated around 17 April 2018 (Liu *et al.* 2018; Neal *et al.* 2018; Chen *et al.* 2019). The volcanic activity caused an increase in pressure at Pu'u 'Ō'ō and subsequent collapse of the crater floor on 30 April 2018, subsequently the lava lake at Pu'u 'Ō'ō started to drain on 2 May 2018. Starting on 1 May 2018, a seismic swarm migrated eastward from Pu'u 'Ō'ō. On 3 May 2018, a dyke intrusion and fissure eruption initiated in the Leilani Estates subdivision along the ERZ, which was captured by continuous GPS (cGPS) observations (Fig. 1). Rapid summit deflation and dilation along the lower ERZ coincided with the onset of a seismic swarm to the southeast of the ERZ, including events near the décollement fault underlying the south flank of Kīlauea (Fig. 1).

On 4 May 2018, the *M*6.9 earthquake occurred 16 km SW of Leilani Estates, as a result of thrust faulting on the shallowly dipping décollement below Kīlauea's south flank (Bai *et al.* 2018; Lay *et al.* 2018; Liu *et al.* 2018). Afterwards, the seismic activity migrated to the west of the *M*6.9 epicentre, involving three main clusters, including a dense cluster around the Kīlauea summit caldera (Fig. 1). The *M*6.9 earthquake is the largest event in Kīlauea's south flank since the 1975 Kalapana *M*7.7 earthquake (Ando 1979). Liu *et al.* (2018) argue that the May 4 earthquake may have been triggered by either the dyke intrusion along the ERZ, or by a sequence of foreshocks, including a thrust-faulting *M*5.4 event that occurred one hour before the main shock.

For about 3 months after the *M*6.9 event, multiple fissures erupted continuously along Kīlauea's ERZ in the Leilani Estates subdivision (Neal *et al.* 2018). The eruption-earthquake sequence has also been associated with caldera roof collapse events and ash explosions at Halema'uma'u crater in the summit caldera, accompanying rapid subsidence of the summit region and caldera. The post-earthquake sequence of events was accompanied by large-scale deformation along a linear zone of intense subsidence along the ERZ (Fig. 1) captured by radar interferograms and data from the ground based cGPS network in the region, which we investigate in the subsequent section.

3 DATA AND METHODS

In order to characterize the deformation associated with the 4 May 2018 *M*6.9 earthquake and dyke intrusion events, we have considered InSAR data from two Sentinel-1 interferograms including the *M*6.9 main shock (i.e. 05/02/2018 to 05/08/2018 for ascending track T124 and 04/23/2018 to 05/05/2018 for descending track T87). To quantify the surface deformation due to magmatic activity beneath the Kīlauea summit caldera in the days prior to the *M*6.9 earthquake, we consider InSAR interferogram between 04/20/2018 and 05/02/2018. The InSAR data were processed with Generic Mapping Tools Synthetic Aperture Radar (GMTSAR, Sandwell *et al.* 2011). For each track, all images were aligned to a single master with geometrical alignment method using precise orbits and a Digital Elevation Model (DEM) (Wang *et al.* 2017; Xu *et al.* 2017). We used 1-arcsec (∼30 m ground resolution) Shuttle Radar Topography Mission (SRTM) for the geometric alignment and the

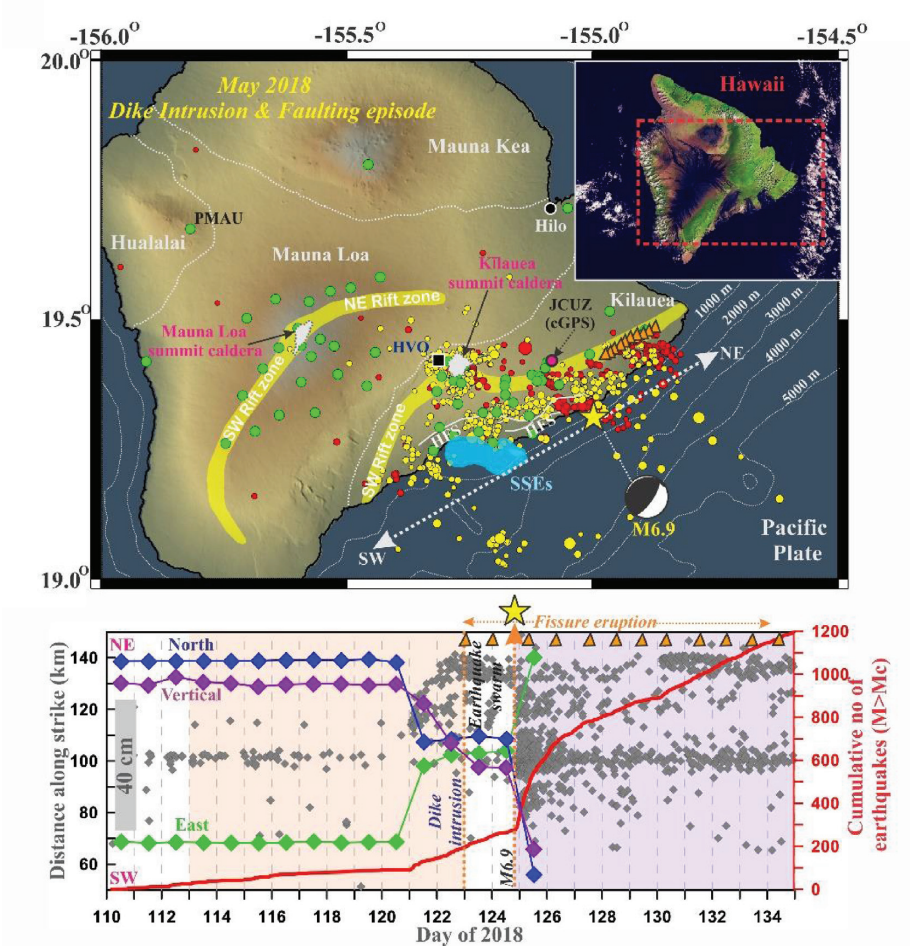

Figure 1. General Tectonics and May 2018 dyke intrusion on Kīlauea's East Rift Zone. Top panel: inset with red box shows the region of Hawaii Island considered in this study. Green dots are the cGPS stations. The yellow star corresponds to the location of the *M*6.9 earthquake and its W-phase focal mechanism solution from USGS (https://earthquake.usgs.gov/earthquakes/eventpage/us1000dyad#moment-tensor). Red and yellow circles show earthquakes ($M > M_c$, $M_c = 2.0$, from US Geological Survey) from 14 d before and until 11 d after the *M*6.9 event, respectively. Orange triangles mark the location of 2018 fissure eruptions along the ERZ. Region of historic slow-slip events (SSEs) is indicated by light blue patch (Foster *et al.* 2013). Rift zones of Mauna Loa and Kīlauea are indicated by yellow patches, along with their summit calderas (represented by grey patches). The depth-labeled white dotted contours represent bathymetry contours. (*Bottom panel*) Seismicity of $M > 2$ (grey diamonds) from 20th April (JD 110) to 15th May (JD 135), 2018 projected along strike distance of the Kīlauea rift zone (white dashed line with double arrow in upper panel) and its corresponding cumulative number curve (red line). Orange shaded region marks the time period 10 d before the initiation of intrusive activity (JD 113 through 123) along the Leilani Estates subdivision and blue shaded region represents 10-d period following the earthquake (JD 125–135). Colored diamonds indicate displacement time-series of cGPS site (JCUZ, marked in top panel) near to the ERZ. Note two distinct patches of earthquakes associated with the rifting process and aftershocks, one following the dyke intrusion and the other near the *M*6.9 event. HVO, Hawaiian Volcano Observatory; HFS, Hilina Fault System.

topographic phase removal. The real and imaginary parts of the original interferometric phase were first filtered with a Gaussian filter of 0.5 gain at a wavelength of 90 m, which were further filtered by a modified Goldstein filtering in the frequency domain with $\alpha = 0.5$ (Goldstein & Werner 1998). After masking out the pixels with correlation lower than 0.1, we unwrapped the phase using the Statistical-Cost Network-Flow Algorithm for Phase Unwrapping (SNAPHU) (Chen & Zebker 2000) and used the nearest neighbor interpolation method to facilitate the unwrapping (Agram & Zebker 2009). We visually inspected all unwrapped interferograms to ensure there were no obvious phase jumps due to unwrapping errors. To mitigate atmospheric artefacts, we removed the best fitting linear dependence of the radar phase on topography from each interferogram, using pixels outside of the Kīlauea region where the surface deformation due to the magma intrusion and the *M*6.9 earthquake is expected to be small. We acknowledge that for both ascending (T124) and descending (T87) tracks, some residual atmospheric noise due to the turbulent part of atmospheric perturbation may still remain, which may lead to variable fringe rates in the corrected interferogram whose contribution is quiet insignificant.

In order to represent a robust constraint on the coseismic deformation process and deformation prior to the May 2018 volcano-tectonic episode, in addition to the Sentinel-1 InSAR we considered cGPS observations from the Hawaiian geodetic network (Montgomery-Brown *et al.* 2015). The USGS Hawaiian Volcano Observatory, University of Hawaii, Stanford University, the Jet Propulsion Laboratory, U.S. Coast Guard and Federal Aviation Authority have been operating this dense cGPS network on Kīlauea and Mauna Loa volcano and associated rift zones (Fig. 1). About 57 cGPS sites of 5-min solutions archived from the Nevada Geodetic Laboratory (Blewitt *et al.* 2018) have been used to capture the coseismic deformation surrounding the Kīlauea Volcano. Moreover, in order to understand magma reservoir inflation and décollement slip preceding the *M*6.9

and dyke intrusion event, we have considered cGPS velocities for the period of 2013–2018.

We inverted the coseismic offsets and interseismic velocity field observed at cGPS sites (with respect to cGPS site PMAU) on Hawaii to characterize the décollement slip in the rupture zone of the 4 May 2018 *M*6.9 earthquake. We considered a uniform dip angle (7°) and strike (239°) of the rupture zone (Liu *et al.* 2018) and divided the fault plane into 260 subfaults (20 along strike × 13 along dip) of size 3 × 3 km^2. We adopted the inversion scheme of Wang *et al.* (2009) which involves a steepest descend optimization approach to search for the optimal values of slip and slip-direction on each subfault. We used the Green's functions for rectangular dislocations in an elastic half-space earth model derived by Okada (1992). The objective function is defined by the following expression:

$$F(s) = \|Gs - u\|^2 + \alpha^2 \|L\tau\|^2, \quad (1)$$

where L is the finite difference approximation of the Laplacian operator, τ is the variability of shear stress drop or roughness which depends on slip magnitude, α is the smoothing parameter, G represents the Green's functions relating unit slip on each patch to displacements at each observation point, u contains the observed GPS displacements and s is the slip on each fault patch to be solved. The smoothing parameter depends on the trade-off curve of the roughness and relative misfit between data and model. We derived an optimal value of the smoothing parameter of 0.2 and used it to derive the dislocation slip model of the May 2018 earthquake and the rate of decollement slip prior to the earthquake (Figs S1 and S2).

To represent the volcano-earthquake interaction prior to the May 2018 dyke intrusion events, we quantify the surface deformation caused by two magma reservoir sources; that is Kīlauea and Mauna Loa (Yang *et al.* 1988). Surface deformation induced by these two magma reservoirs are modelled by considering spherical magma sources in an elastic half-space using the dMODELS software package (Battaglia *et al.* 2013). We adopted the inversion approach of Battaglia *et al.* (2013) to derive the rate of magma inflation and surface deformation at GPS sites surrounding the Kīlauea and Mauna Loa summits and magma chambers. We have considered a spherical magma chamber, embedded in a homogeneous, isotropic, elastic and flat half-space, having a radius (a) of 500 m and source depth (z_0) of 5 km for both, Kilauea and Mauna Loa. The rate of magma inflation depends on four parameters: the dimensionless pressure change ($\Delta P/\mu$, where μ is the shear modulus), and the source location and depth (x_0, y_0, z_0). The change in the volume (ΔV) of the spherical magma reservoir is defined by (McTigue 1987; Battaglia *et al.* 2013):

$$\Delta V = \pi a^3 \frac{\Delta P}{\pi} \left[1 + \left(\frac{a}{z_0} \right)^4 \right]. \quad (2)$$

Further, in order to quantify the deformation in the days leading up to the 4 May 2018 *M*6.9 earthquake, we have jointly inverted the Sentinel-1 InSAR data and 5-min solutions of GPS displacements from the Nevada Geodetic Laboratory spanning 04/20/2018 to 05/02/2018 for opening and closing of the magmatic dyke system along the ERZ.

4 RESULTS

4.1 May 2018 dyke intrusion and décollement faulting: constraints from geodetic observations

In order to probe the surface deformation associated with the May 2018 dyke intrusion and décollement faulting, we analysed coseismic deformation derived from both GPS and InSAR observations. We selected two Sentinel-1 interferograms spanning the *M*6.9 main shock with relatively low atmospheric noise (05/02/2018 to 05/08/2018 for ascending track T124 and 04/23/2018 to 05/05/2018 for descending track T87). Both interferograms include surface displacements due to the May 4 *M*6.9 earthquake and deformation due to rifting along the ERZ and withdrawal of magma from the summit reservoir (Fig. 2, top panel). LOS displacements from both ascending and descending tracks exhibit significant range increase (up to >25 cm) over the caldera and much of the ERZ, indicative of surface subsidence as a result of the magma drainage and transport to eruptive fissures near Leilani Estate. Two representative profiles across the East rift zone (A–A') and the Kīlauea caldera (B–B') also indicate significant ground subsidence (Fig. 2, bottom panel) along the southern flank of the ERZ and the summit caldera. Along the coast, the opposite signs of LOS displacements (negative for ascending track T124 and positive for descending track T87) document significant horizontal motion, which is mainly due to the *M*6.9 main shock.

The coseismic offsets from 57 cGPS stations surrounding the Kīlauea Volcano document up to 0.77 m of horizontal motions and reveal strong gradients in the displacement field, indicating extensional strain across the ERZ. We inverted the cGPS-derived coseismic offsets for the *M*6.9 earthquake and generated a finite-fault model for the coseismic slip along the décollement fault. For this model, we did not include the Sentinel-1 InSAR data since the coseismic SAR interferograms span significant periods of post-earthquake and pre-earthquake deformation (i.e. magma transport and dyke intrusion). So, combining the GPS displacements along with the InSAR data would significantly reduce the robustness of the coseismic displacement model. Therefore, we have only inverted the GPS displacements from the 5-min solution. We calculated the Green's functions relating fault slip to surface displacement using rectangular dislocations (Okada 1992) in a homogenous elastic half-space. We implemented the inversion scheme of Wang *et al.* (2009), involving a steepest descent approach in the constrained least-square optimization. We estimated the slip distribution on the rupture plane, adopting the fault geometry reported by Liu *et al.* (2018). Liu *et al.* (2018) present a kinematic finite-slip model derived from joint inversion of teleseismic waves, strong-motion data and coseismic GPS offsets. They find that the *M*6.9 earthquake occurred on the décollement dipping 7° landward with slip of up to 3.0 m and a low average rupture speed (∼1 km s^{-1}). Morgan *et al.* (2000, 2003) have identified the average dip of the décollement as ∼2–3° in offshore reflection images. Liu *et al.* (2018) argue that the actual dip may in fact exceed that of the décollement and possibly some or the entire coseismic slip may involve a steeper splay fault. A steeper splay thrust has been identified in offshore reflection profiles (Hills *et al.* 2013) and may have been activated during the *M*6.9 event. Lay *et al.* (2018) compare models using 7.5° and 3° dipping rupture plans and find that the shallower dip results in a landward shift of inverted slip and a modestly worse fit to seismic and GPS observations.

We discretized the rupture zone on the décollement fault into 3 × 3 km^2 subfaults for the distributed slip inversion and chose an

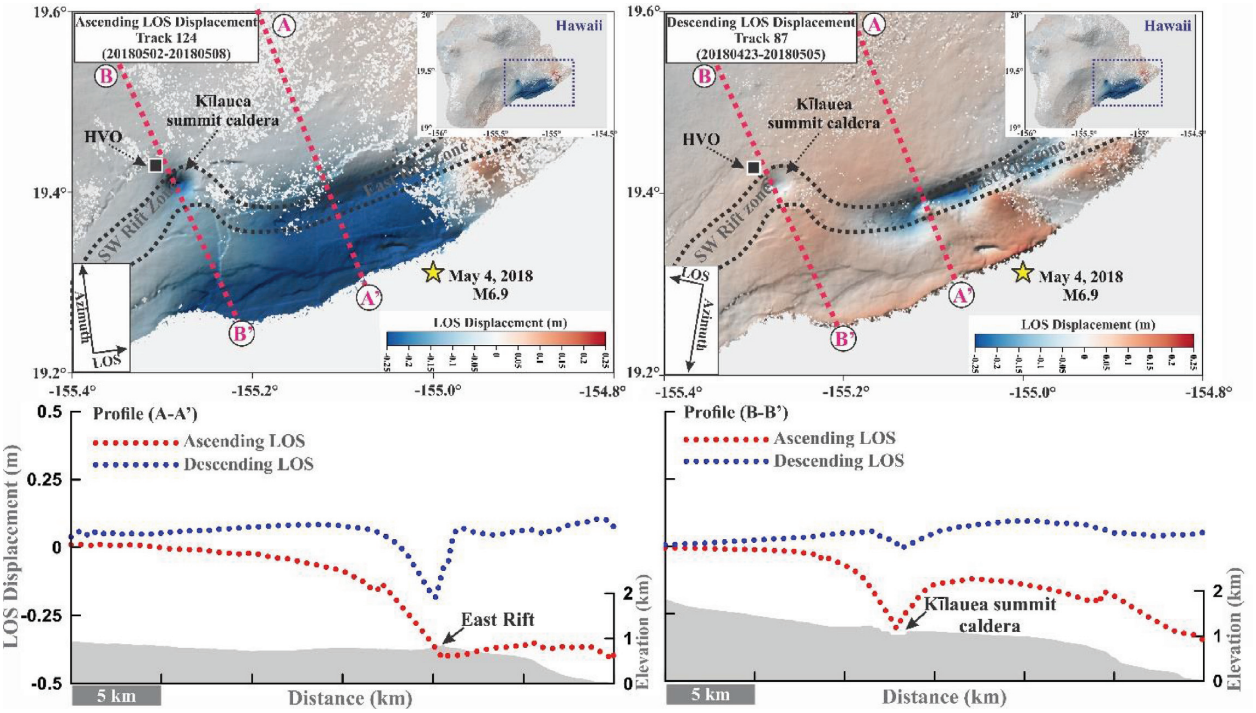

Figure 2. InSAR LOS displacements (positive towards the satellite) over Hawaii (inset) obtained along two Sentinel-1 satellite tracks, after removal of atmospheric noise. The region marked by dotted rectangle in the inset has been enlarged. LOS displacement of the ascending track 124 (top left-hand panel) and LOS displacement of the descending track 87 (top right-hand panel), include surface displacements associated with the 4 May 2018 *M*6.9 earthquake as well as the magmatic activity during the respective 6- and 12-d image acquisition intervals (indicated in top left of the maps). Two representative profiles (A–A' and B–B') for both ascending and descending LOS displacement are presented in the bottom panel. Hawaiian Volcano Observatory (HVO) is marked by the black square, while the rift zone is outlined by dashed black lines.

optimal smoothing factor of 0.2 based on the trade-off curve between the roughness of shear stress drop of the model and the fitting residual (Fig. S1). The estimate of average RMS misfit between the observed and calculated horizontal and vertical coseismic displacements for our preferred slip model is 4.1 cm. Figs 3 and S3 shows the finite-fault models derived from our inversion of the coseismic GPS displacements (Figs 3a and b) and the kinematic slip model proposed by Liu *et al.* (2018) (Figs S3a and b). Both models (Figs 3 and S3) indicate maximum slip of ∼2.5–3.0 m, with an average slip of about 0.8–0.9 m on the décollement fault surface south of Kīlauea's ERZ. The simulated 3-D coseismic offsets in our rupture model (Figs 3a and b), are in somewhat better agreement with the GPS measurements than the offsets from the model proposed by Liu *et al.* (2018) (Figs S3a and b), with a RMS misfit of 4.8 cm. However, Liu *et al.* (2018) argue that combining seismic data and coseismic GPS offsets provides better sensitivity to details of the offshore source process.

4.2 Long-term deformation prior to the May 2018 eruption-earthquake sequence: constraints from cGPS observations

In order to understand how magma reservoir inflation and décollement slip driven by gravitational stresses evolved prior to the recent May 2018 volcano-tectonic episode, we considered cGPS derived velocity estimates for 2013–2018 from the Hawaiian geodetic network (Montgomery-Brown *et al.* 2015). By selecting this time period, we have excluded the effects of the Kamoamoa eruption in 2011 (Lundgren *et al.* 2013; Baker & Amelung 2015). However, during this period one slow slip event on the décollement in 2015 contributed to the deformation (Montgomery-Brown *et al.* 2015). Therefore, we consider the average velocities spanning this time period in our modelling. The average velocity estimates from 2013 to 2018 are computed relative to PMAU, a cGPS station located in the Hualalai region that is far from the May 2018 dyke intrusion and faulting events. The surface displacements around the Kīlauea summit caldera, ERZ and adjacent décollement region reflect a complex strain accumulation process. The cGPS data indicate that the south flank of Kīlauea volcano, which has hosted several large historic earthquakes on its basal décollement (Ando 1979; Dieterich *et al.* 2000; Owen & Bürgmann 2006), is showing motion up to ∼8 cm yr^{-1} (with an average rate of ∼4 cm yr^{-1}) to the south-southeast (Fig. 4). It appears that the Kīlauea summit caldera zone has been rising with a maximum uplift rate of ∼9 cm yr^{-1} (with an average rise of ∼5 cm yr^{-1}), along with radial near-field displacements (∼6 cm yr^{-1}) away from the centre of the magma reservoir (Fig. 4). Similar radial near-field displacements of ∼6 cm yr^{-1} are also observed around Mauna Loa summit caldera (Fig. 4a), with an overall uplift rate of ∼3.5 cm yr^{-1} (Fig. 4b).

In order to represent the complex deformation prior to the May 2018 dyke intrusion, we implemented an inversion of the cGPS-derived velocity estimates, by combining distributed slip on elastic dislocations in a homogeneous elastic half-space (Okada 1992) and two spherical magma reservoir sources at both Kīlauea and Mauna Loa (Yang *et al.* 1988). We extended the fault geometry towards the southwest of the coseismic rupture model of the *M* 6.9 earthquake (Liu *et al.* 2018), in order to capture deformation along the full extent of the south flank detachment. Again, we discretized the fault into smaller elements (3 × 3 km^2). Surface deformation due to an expanding magma reservoir at the Kīlauea summit caldera

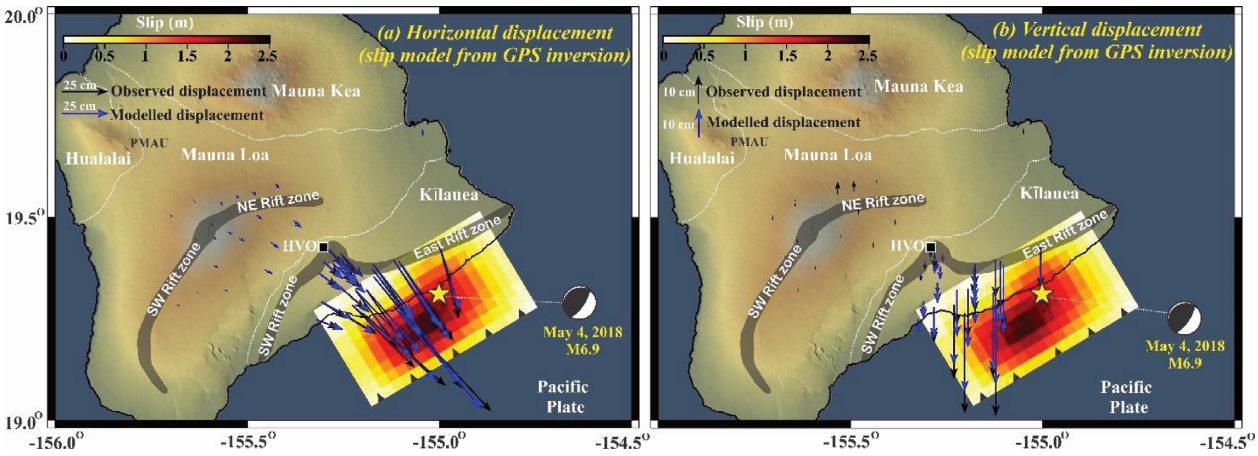

Figure 3. Coseismic GPS displacements due to the 4 May 2018 *M*6.9 earthquake and associated finite fault models. The 4 May 2018 *M*6.9 earthquake and slip model for both horizontal (a) and vertical (b) displacements, derived from the inversion of coseismic offsets from the cGPS time-series sampled at 5-min intervals. The RMS misfits of the slip models is 4.1 cm.

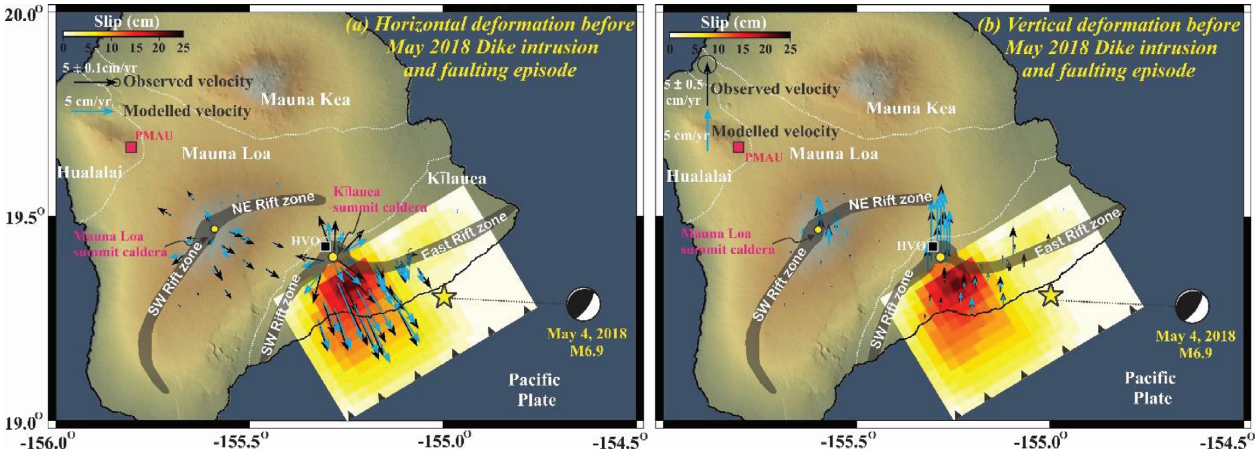

Figure 4. Inversion to model cGPS derived average velocity during 2013–2018, combining elastic dislocation model and spherical magma sources for both Kīlauea and Mauna Loa magma reservoir. (a) Observed horizontal velocities (black arrows) across the décollement surface and surrounding the spherical magma sources (marked by yellow circles), with respect to the site PMAU. Sky blue arrows indicate predicted GPS velocities due to slip along the décollement surface and surrounding the spherical magma sources. (b) Vertical velocities show an overall uplift surrounding both the Kīlauea and Mauna Loa magma summits that are consistent with the model predictions. Error ellipse on the scale arrows shows 95 per cent confidence level and the uncertainties of all sites are comparable.

region is modelled with spherical magma reservoir sources in an elastic half-space using the dMODELS software package (Battaglia *et al.* 2013). As we hold the source dimension fixed to a 500 m radius, the solution for the spherical magma source depends on its location (latitude, longitude and depth) and the dimensionless pressure change $\Delta P/\mu$, where $\mu = 30$ GPa is the shear modulus (Battaglia *et al.* 2013). Table S1 summarizes the list of modelled parameters to represent the summit reservoir deformation that are considered in the present inversion approach. We also tested other source models for the caldera inflation, such as a spheroid and sill, and found that the data fitting from those models is no better than the spherical magma source. In this inversion, we apply an optimal smoothing parameter of 0.2 that balances the roughness of shear stress drop on the décollement with the reduction in data misfit (Fig. S2). The RMS residual of the preferred model shown in Fig. 4 is 2.0 cm.

Overall, predictions of the surface displacement with optimal model parameters fit the observations near the summit reasonably well (Figs 4a and b). The model that yields the lowest misfit to the data contains spherical magma inflation sources near the summit caldera of Kīlauea and Mauna Loa with magma inflation of 9.22×10^6 and 4.76×10^6 m^3 yr^{-1}, respectively, at depth of 5 km (Figs S4 and S5). These results are consistent with the findings of Chen *et al.* (2019), in which they used combined geodetic, seismic, and tsunami observations to model triggering of the *M*6.9 Hawaii earthquake and dyke intrusion activity. During the 2013–2018 observation period, little slip was found on the portion of the basal detachment that ruptured during the 2018 *M*6.9 earthquake (Figs 3 and 4). Therefore, elastic modelling of the cGPS data suggests that the active sources of deformation during the decade preceding the *M*6.9 earthquake includes slip on the sub-horizontal décollement away from the coseismic rupture and inflation near the summit caldera (Fig. 4). The lack of cGPS coverage around and to the north of the ERZ does not allow us to constrain the likely contribution of deep rift opening to the deformation (Owen *et al.* 2000a).

We suggest that the recent long-term deformation episode prior to the May 2018 dyke intrusion is different from the 1990–1996 period of rapid deformation of Kīlauea Volcano (Owen *et al.* 2000a).

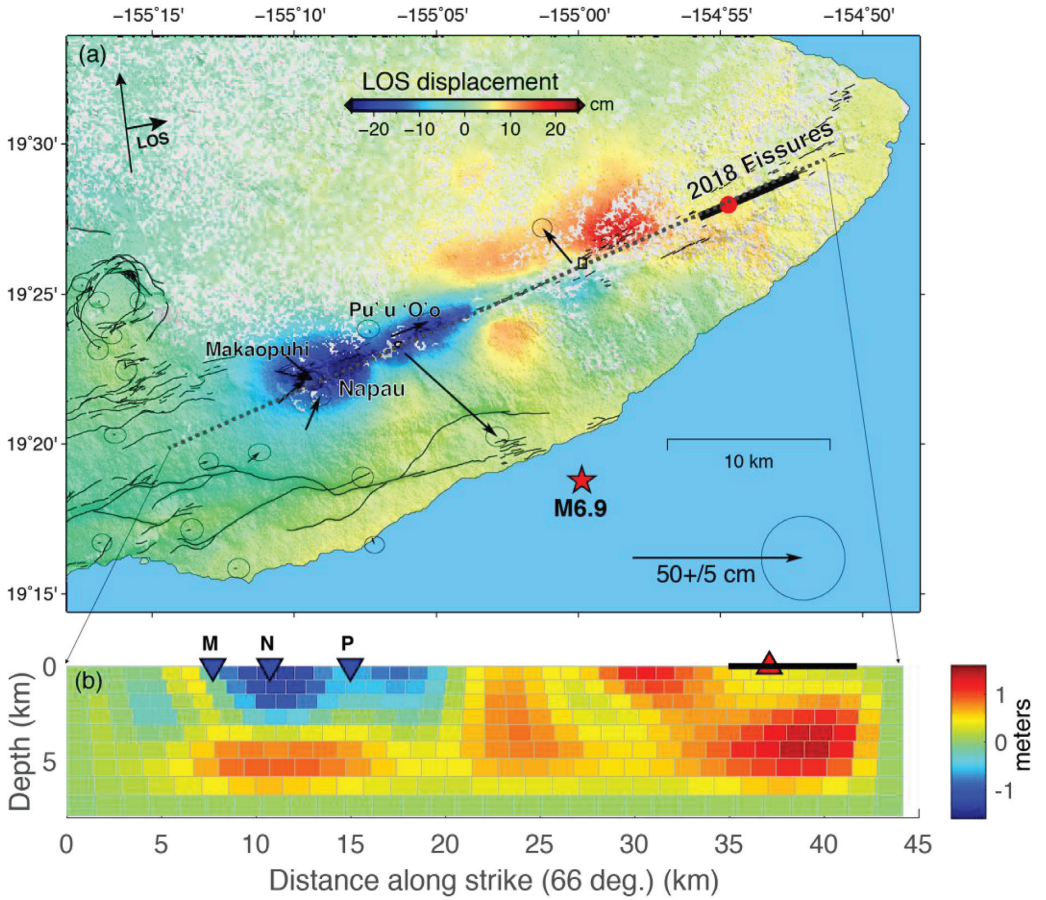

Figure 5. Pre-earthquake surface deformation. Top panel: LOS displacements between 04/20/2018 and 05/02/2018 derived from Sentinel-1 observations along the ascending track T124. Positive values correspond to surface motion toward the satellite. Vectors represent horizontal GPS displacements derived 5-min solutions during the InSAR observation period. Positions within a 3-hr window around the SAR image acquisition time are averaged to increase the signal to noise ratio. Bottom panel: dyke model derived from InSAR and GPS displacements shown in the top Fig. M = Makaopuhi; N = Nāpau; P = Pu'u 'Ō'ō. Negative opening uprift of Pu'u 'Ō'ō reflects transport of magma towards the eventual eruptive fissures at Leilani Estates that began to erupt one day following the observation period (black bar).

During 1990–1996, campaign GPS measurements show that the summit and surrounding rift zones subsided with maximum subsidence rates of ∼8 cm yr^{-1} (Owen *et al.* 2000a), whereas the summit region has been rising with a maximum uplift rate of ∼9 cm yr^{-1} during 2013–2018 (Fig. 4b). Horizontal velocity estimates during the recent time period show a radial pattern of motion away from the inflating magma sources (Fig. 4a). However, the geodetic observations by Owen *et al.* (2000a) showed no such radial displacement surrounding the Kīlauea summit caldera. Southeast-directed station velocities south of the ERZ, approaching ∼7 cm yr^{-1} near the coast, are consistent with décollement slip and deep rift opening at >20 cm yr^{-1} during the early 1990 s (Owen *et al.* 2000a, Fig. S6).

4.3 Short-term deformation leading up to the May 4 *M*6.9 earthquake

As described earlier, intense magmatic activity beneath the summit caldera and along much of the ERZ started days before the *M*6.9 earthquake, which produced significant deformation at the surface. Fig. 5 shows the Sentinel-1 InSAR LOS and GPS displacements between 04/20/2018 and 05/02/2018. Surface deformation during this period is characterized by significant subsidence and contraction along the Makaopuhi-Pu'u 'Ō'ō section of the ERZ, and expansion along the adjoining downrift sections. During this period, only subtle surface deformation is seen along the eventual 2018 Leilani Estates eruptive fissures, indicating that the dyke emplacement and magma transport were still ongoing before the fissures finally erupted one day later on 3 May 2018.

To investigate the effect of the pre-earthquake magmatic intrusion on the basal detachment that hosted the *M*6.9 earthquake, we modelled the surface deformation immediately prior to the earthquake with a series of tensile dislocation patches assuming that the surface deformation can be approximated by either dyke opening or closing (Fig. S7). For simplicity, we assumed a uniform strike of 66° that best matches the surface fracture traces of the ERZ. The ∼44-km-long and 8-km-wide model was divided into rectangular patches whose length and width increase with depth (Fig. 5). Each patch was allowed to have either opening or closing in the range of –5 to 5 m. We downsampled the InSAR LOS displacements iteratively using the quad-tree curvature-based algorithm applied to the model predictions in each round to avoid oversampling in noisy areas (Wang & Fialko 2015). In addition to InSAR LOS displacements, we also included GPS displacements corresponding to the InSAR observation period that were derived from the Nevada Geodetic Laboratory 5-min solutions. To enhance the signal-to-noise (SNR), positions 3 hours before and after the corresponding SAR image acquisition times were averaged and then differenced to compute

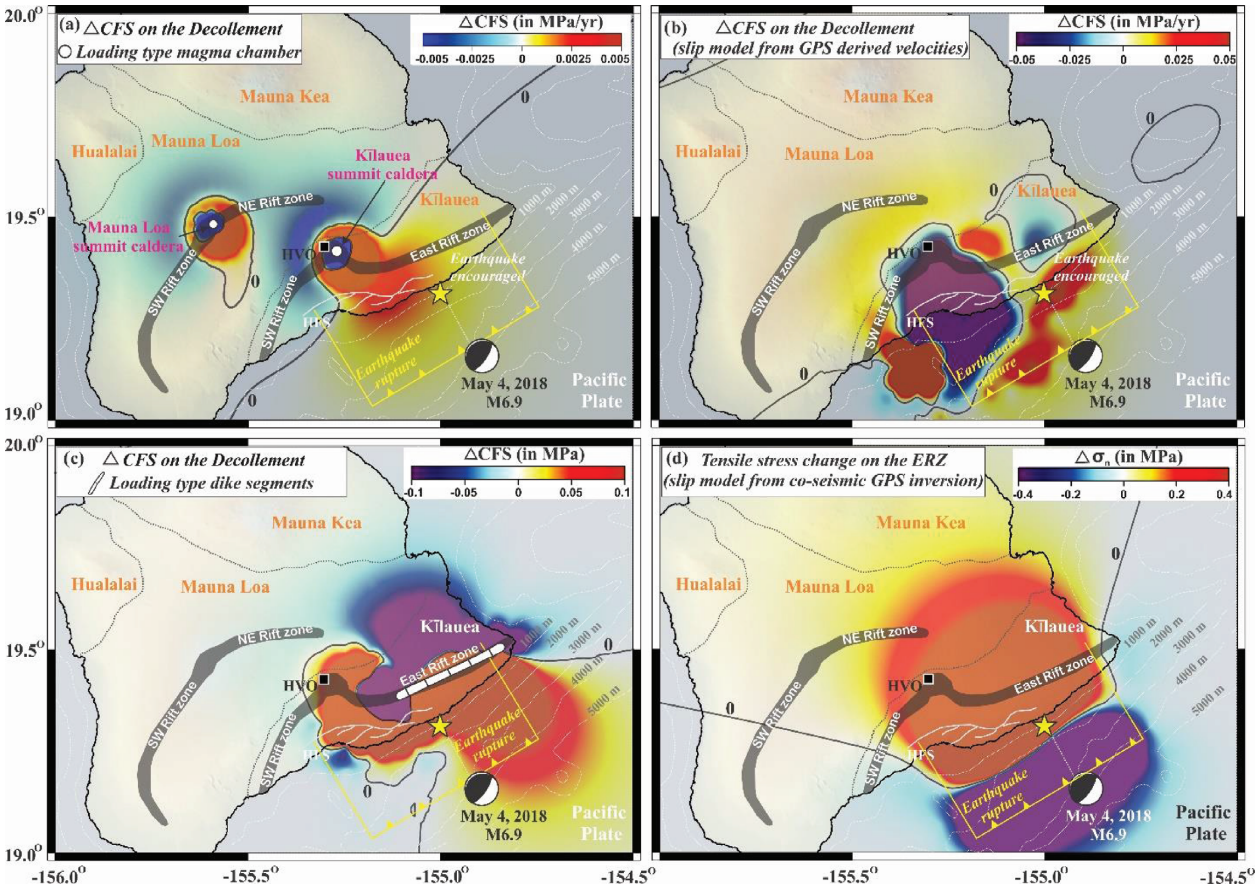

Figure 6. Earthquake-volcano interaction cycle on Kīlauea's ERZ. (a) Mean annual change in Coulomb failure stress (ΔCFS) due to 2013–2018 magma reservoir inflations at 5 km depth for both Kīlauea and Mauna Loa reservoirs resolved on the décollement surface (239°,7°,114°) at a depth of 5 km. The magma inflation points are marked by white circle. (b) ΔCFS on the décollement surface at 5 km depth, from rapid fault creep on the décollement, derived from the slip model from GPS derived mean velocities for 2013–2018 (Fig. 4). Note, the earthquake epicentre lies in the zone of positive Coulomb stress change, which implies the magma inflation and décollement creep encouraged the earthquake. (c) ΔCFS computed on the décollement surface at 5 km depth, due to 2018 dyke intrusion on the ERZ. The opening along the ERZ is derived from inversion of pre-earthquake InSAR interferogram (04/20/2018–05/02/2018, Fig. 5). (d) Change in tensile stress ($\Delta\sigma_n$) computed at 2 km depth on the Kīlauea's ERZ due to the 4 May 2018 *M*6.9 earthquake. The tensile stress change is computed by using the slip model derived from inversion of coseismic GPS offsets, shown in Fig. 3(a). Note that the earthquake epicentre of the May 4, *M*6.9 faulting episode lies in the zone of positive Coulomb stress change. This shows that the shallow magma reservoir source, rift intrusions and décollement creep caused positive stress change on locked sections of the décollement surface, and in turn the May 4, *M*6.9 faulting episode caused stress change on the magma reservoir and the ERZ, implying a cyclic interaction between volcano and faulting processes.

the GPS displacements during the InSAR observation period. The preferred dyke model for the 12-d period is shown in Fig. 5. The model is characterized by ∼1.5 m closing at shallow depth (<3 km) between Makaopuhi and Pu'u 'Ō'ō, and ∼1 m opening along the section between Pu'u 'Ō'ō and the 2018 Leilani fissures (Fig. 5b). This is consistent with transport of magma from the ERZ section uprift of Pu'u 'Ō'ō feeding the dyke intrusion growing downrift towards Leilani Estates. The corresponding dyke model was then used to compute the stress change on the fault plane of the *M*6.9 earthquake (Fig. 6c).

5 DISCUSSION

5.1 Earthquake-volcano interaction cycle on Kīlauea: implications from stress transfer models

Here, we invoke an earthquake-volcano interaction cycle and associated static stress transfer in the recent 2018 episode on Kīlauea's ERZ. For this, we examined the static stress changes from pre-earthquake stress loading (i.e. by magma reservoir inflation, rapid secular fault creep on the décollement downdip of the rupture and dyke intrusion on the ERZ) on the coseismic rupture surface (Figs 6a, b and c) and the coseismic stress loading (i.e. by the coseismic slip of 4 May 2018 *M*6.9 earthquake) on the rift and how that might have affected the subsequent development of the eruption sequence (Fig. 6d). We present Coulomb failure stress change and tensile stress in cross-section view across the décollement surface in Fig. 7, incorporating the 4 May 2018 *M*6.9 earthquake epicentre.

Assuming deformation in an elastic half-space (Okada 1992), the static Coulomb failure stress change ($\Delta CFS = \Delta\tau + \mu'\Delta\sigma_n$) is computed, where $\Delta\tau$ is the shear stress change along the slip vector on a given plane (positive sign represents in slip direction), $\Delta\sigma_n$ is the normal stress change (positive sign represents for unclamping), and μ' is the effective coefficient of friction (Cocco & Rice 2002). The estimated ΔCFS depends on the specific source model and the geometry (i.e. strike and dip), rake and friction coefficient of the considered 'receiver' faults (i.e. shallowly dipping décollement

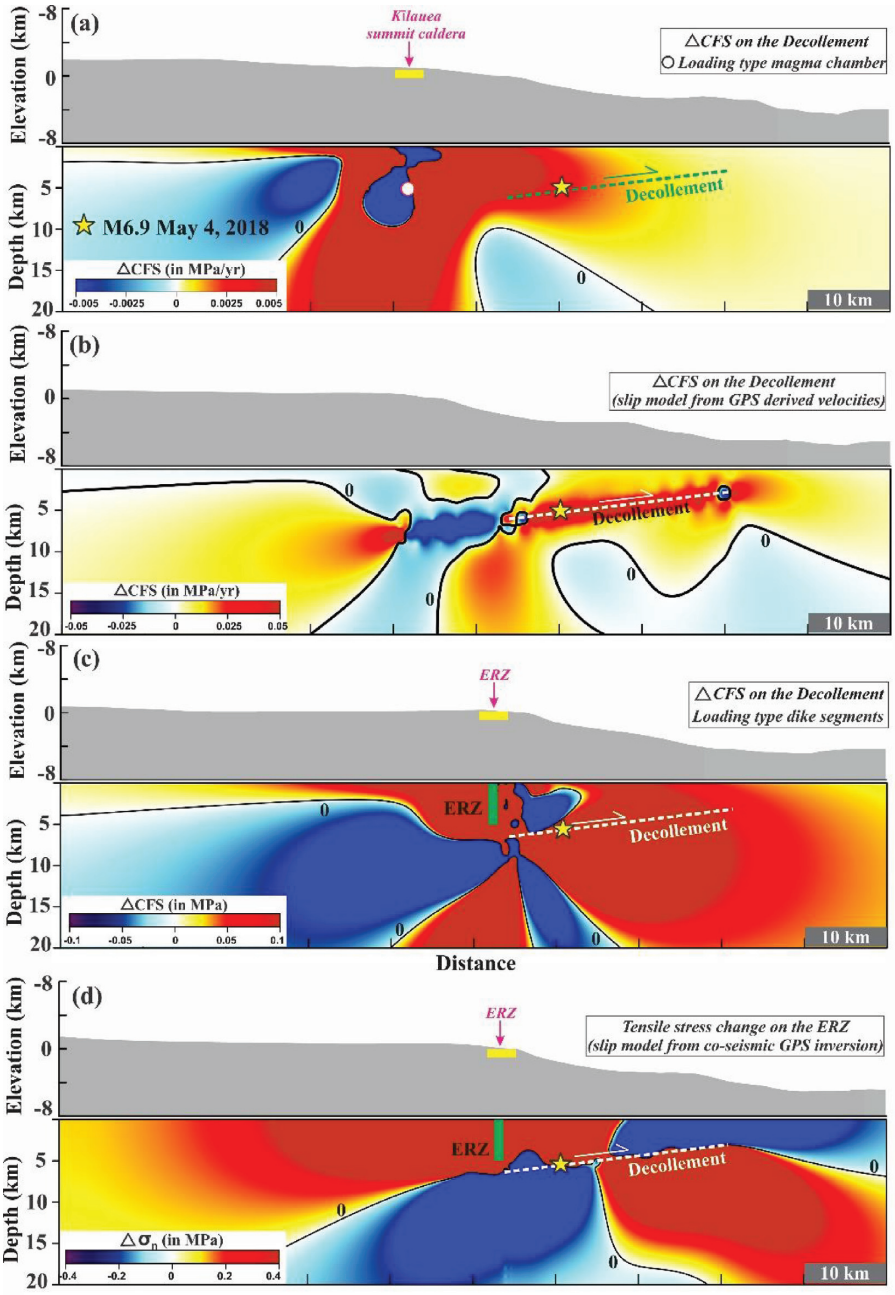

Figure 7. Change in Coulomb failure stress on the décollement surface and change in tensile stress on the ERZ. Panels (a), (b) and (c) show change in Coulomb failure stress on the décollement surface due to magma inflation, coseismic slip and dyke intrusion on the ERZ, respectively. White dashed line shows the décollement surface with 7° dip. Note that in each case the earthquake epicentre lies in the zone of positive stress changes. Panel (d) show change in tensile stress on the ERZ due to coseismic displacement during the earthquake event. Note that the ERZ lies in the positive tensile stress zone, which indicates rift opening is influenced by the coseismic slip.

surface or steeply dipping rift structure) on which the ΔCFS are resolved (Freed 2005). For dyke receiver structures along the rift zones, we compute the tensile stress changes ($\Delta\sigma_n$).

The ΔCFS is computed by considering the two magma reservoir inflation sources for both Kīlauea and Mauna Loa at ∼5 km depth with magma inflation of 9.22×10^6 and 4.76×10^6 m^3 yr^{-1}, respectively (Fig. 6a) and an effective friction coefficient $\mu' = 0.4$ on the décollement. We resolved the stress changes for points at 5 km depth on the décollement fault geometry proposed by Liu *et al.* (2018) (i.e. with strike 239°, dip 7° and rake 114°) which is consistent with previous studies (Owen *et al.* 2000a; Dieterich *et al.* 2003; Owen & Burgmann 2006). Fig. 6(a) shows that the magma reservoir inflation sources encourage faulting on the décollement, including the source region of the 2018 *M*6.9 earthquake, with stressing rates of ΔCFS of 0.0025–0.005 MPa yr^{-1} (Figs 6a and 7a). This supports the concept that the faulting episodes along the décollement are a consequence of stress transfer by the expansion of the subsurface magma reservoir at the Kīlauea summit caldera. In fact, a similar kind of stress transfer mechanism has been proposed at Mauna Loa and Kīlauea volcanos and surrounding rift zone for previous earthquakes on the décollement (Dieterich 1988; Dieterich *et al.* 2000; Walter & Amelung 2006).

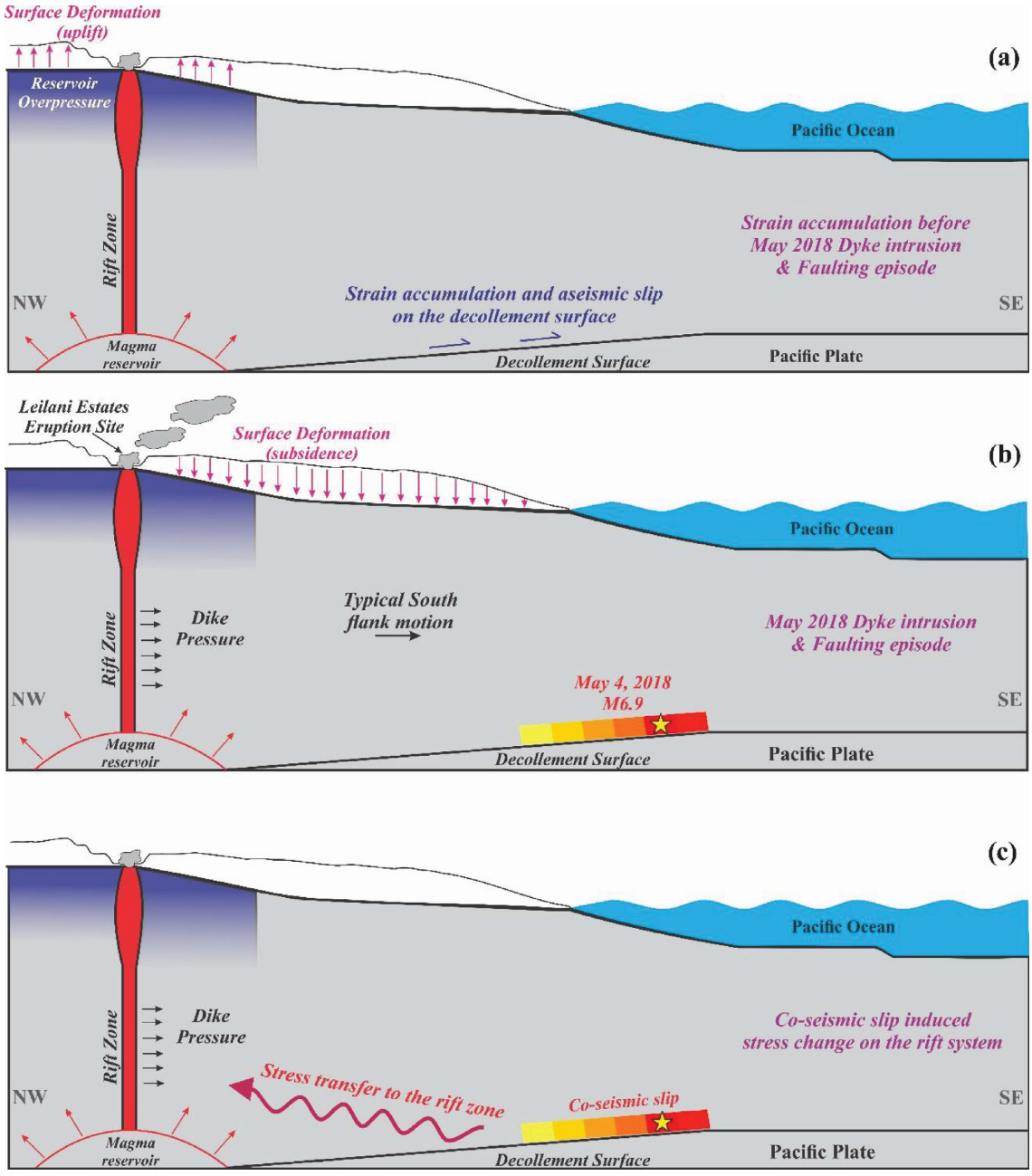

Figure 8. Schematic profile across the south flank of Kīlauea caldera showing the influence of dyke intrusion and associated faulting episode. (a) Schematic NW-SE cross-section representing deep source magma pressurization. This creates overpressure in the reservoir resulting in surface uplift and causes strain accumulation and aseismic slip on the décollement surface. (b) Represents the onset of volcanic eruption which causes ground subsidence. Initiation of the dyke intrusion and rifting episode causes motion in the southern flank of the rift zone and possibly triggers earthquake (e.g. the 4 May 2018 *M*6.9) along the décollement surface. (c) Represents stress transfer on the rift zone due to the coseismic slip of 2018 May 4, *M*6.9 earthquake.

Further, we have computed ΔCFS on the décollement surface (strike 239°, dip 7°, rake 114°, at a depth of 5 km) due to the rapid secular fault creep downdip of the décollement during the pre-intrusion period for 2013–2018, shown in Figs 6(b) and 7(b). From this, it appears that the earthquake hypocentre of the 4 May 2018 *M* 6.9 faulting episode lies in a zone of positive Coulomb stress change rate (∼0.05 MPa yr^{-1}, Fig. 7b). Further, ΔCFS is computed on the décollement surface at ∼5 km depth, due to 2018 dyke intrusion on the ERZ, derived from the inversion of a pre-earthquake InSAR interferogram (04/20/2018-05/02/2018, Fig. 5). It appears that the earthquake hypocentre of the 4 May 2018, *M*6.9 faulting episode lies in the zone of increased Coulomb stress (∼0.1 MPa, Figs 6c and 7c).

We also computed coseismically induced tensile stress changes ($\Delta\sigma_n$) on Kīlauea's ERZ at a shallow depth of 2 km (Fig. 6d), considering the 4 May 2018 *M*6.9 earthquake rupture model (Fig. 3a) as the source. We find peak tensile stress changes of about 0.4 MPa on the ERZ due to coseismic slip on the décollement (Figs 6d and 7d). The widespread tensile stress change due to the *M*6.9 earthquake may be also responsible for the triggered fault slip across several normal fault systems on the southern flank of the Kīlauea (Wang *et al.* 2019).

From this analysis we infer a cyclic interaction and associated stress change in which the volcanic activity beneath the Kīlauea summit caldera and spreading of the ERZ cause stress change on the décollement surface to trigger the 4 May 2018 *M*6.9 earthquake and previous ruptures of locked sections of the basal detachment. Conversely, the faulting episode on the décollement surface induces strong tensile stress change on the ERZ and the Kīlauea summit caldera (Fig. 8).

5.2 Geodetic data and model limitations

In this study, we have used cGPS derived coseismic and pre-intrusion deformation models to characterize the deformation process during and prior to the 4 May 2018 *M*6.9 earthquake respectively. In addition to that we have jointly inverted the GPS and InSAR observations to define the pre-earthquake surface deformation during the days prior to the *M*6.9 earthquake. Finally, we have used the Coulomb failure stress model to quantify the static stress changes associated with the earthquake-volcano interaction cycle.

The geometry and spatial extent of the ERZ considered in the dyke deformation model are based on previous observations of surface cracks and eruptive fissures (Walter & Amelung 2006). However, the actual position and rate of opening of the rift zone dykes may vary spatially along the strike of the rift zone, and the associated static stress changes may be more heterogeneous and vary locally along the rift zone. Therefore, for simplicity of the model we have considered a uniform dyke opening up to 5 km depth, which is associated with stress concentrations at the dyke edges. Further, in our static stress transfer model we have not considered any deformation related to viscous relaxation of the magmatic source, the lower crust, and/or uppermost mantle (Walter & Amelung 2006). Moreover, we have not explored the role of pore-pressure change in the Coulomb failure stress model. We acknowledge that these factors can be considered as second-order effects in the stress evolution associated with this deformation sequence.

The pre-intrusion geodetic measurements are assumed to reflect the surface deformation caused by tectonic and volcanic processes at depth and are used to estimate the rate of magma inflation for a spherical magma chamber. In the pre-intrusion deformation model, the surface deformation induced by spherical magma source is quantified by an analytical approach (Battaglia *et al.* 2013), which is based on a homogenous, isotropic, elastic flat Earth and half-space assumption.

For InSAR data both satellite tracks (T124 and T87), the first postseismic Sentinel-1 images were acquired days after the *M*6.9 earthquake, coseismic interferograms shown in Fig. 2 contain contributions from both the *M*6.9 earthquake and magmatic activity along the ERZ. For this reason, we did not use the Sentinel-1 InSAR data in the coseismic slip model inversion. On the other hand, the pre-earthquake interferogram shown in Fig. 5(a) provides a valuable data set to constrain the kinematics of the ERZ shortly before the final eruption of the 2018 episode in the lower ERZ, as there are only a handful of GPS sites which have captured the surface deformation during this period. However, we note that due to the relatively poor radar coherence and possibly high atmospheric noise level in Sentinel-1 observations along the vegetated lower ERZ, as well as the 1-D nature of InSAR observations, the dyke model presented in Fig. 5(b) may contain large uncertainties, especially for the deeper part, where the model resolution is expected to be low.

6 CONCLUSIONS

From the above observations, we can summarize that:

(1) A complex volcano-earthquake interaction process is associated with the recent rifting episode along the Kīlauea's East Rift Zone (ERZ) and 4 May 2018 *M*6.9 Leilani earthquake along the décollement surface of Kīlauea's mobile south flank (Figs 8b and c).

(2) Inversion of cGPS data for slip beneath the Kīlauea summit caldera surrounding region suggest a coupled deformation process associated with magma reservoir inflation and aseismic décollement slip driven by gravitational stresses (Fig. 8a), prior to the recent rifting and faulting episodes.

(3) Our inversion of cGPS derived velocity estimates reveals that during the pre-2018 period the eventual coseismic slip patch of the 4 May *M*6.9, 2018 earthquake was devoid of any significant slip.

(4) Further, proposed stress change models due to magma inflation, rapid fault creep on the décollement and coseismic slip of the 4 May *M*6.9, 2018 earthquake imply a complex cyclic interaction of stress change.

ACKNOWLEDGEMENTS

We thank Thorne Lay for providing the finite fault model for the 4 May 2018 Leilani earthquake. GPS displacements are obtained from the Nevada Geodetic Laboratory (NGL, http://geodesy.unr.edu/). Earthquake data are archived from US Geological Survey (https://earthquake.usgs.gov/earthquakes/search/). All the maps and Figures are plotted using GMT software package (version 5.2.1, http://gmt.soest.hawaii.edu/). The static stress change is computed by using Coulomb software package (version 3.3.01, https://earthquake.usgs.gov/research/software/coulomb/). R.B. and K.W. acknowledge support by the NASA ESI program. D.P. was supported by a NITR Research Fellowship. R.K.Y. is thankful to Institute of Seismological Research, Department of Science and Technology, Gujarat, India for the support. This is NGRI publication number NGRI/Lib/2020/Pub-42. We thank Kejie Chen for his comments on an earlier version of the manuscript. We thank the Editor Eiichi Fukuyama, an anonymous reviewer and Kejie Chen for their constructive comments that helped in improve the contents of the paper.

REFERENCES

Agram, P. & Zebker, H., 2009. Sparse two-dimensional phase unwrapping using regular-grid methods, *IEEE Geosci. Remote Sens. Lett.,* **6**(2), 327–331.

Amelung, F., Yun, S.-H., Walter, T.R., Segall, P. & Kim, S.-W., 2007. Stress control of deep rift intrusion at Mauna Loa volcano, Hawaii, *Science,* **316**(5827), 1026–1030.

Ando, M., 1979. The Hawaii earthquake of November 29, 1975: low dip angle faulting due to forceful injection of magma, *J. geophys. Res.,* **84,** 7616–7626.

Bai, Y., Ye, L., Yamazaki, Y., Lay, T. & Cheung, K.F., 2018. The 4 May 2018 MW 6.9 Hawaii Island earthquake and implications for tsunami hazards, *Geophys. Res. Lett.,* **45,** doi:10.1002/2018GL079742.

Baker, S. & Amelung, F., 2015. Pressurized magma reservoir within the east rift zone of Kīlauea Volcano, Hawai'i: evidence for relaxed stress changes from the 1975 Kalapana earthquake, *Geophys. Res. Lett.,* **42**(6), 1758–1765.

Battaglia, M., Cervelli, P.F. & Murray, J.R., 2013. dMODELS: A MATLAB software package for modeling crustal deformation near active faults and volcanic centers, *J. Volc. Geotherm. Res.,* **254,** 1–4.

Blewitt, G., Hammond, W.C. & Kreemer, C., 2018. Harnessing the GPS data explosion for interdisciplinary science, *EOS, Trans. Am. Geophys. Un.,* **99,** doi:10.1029/2018EO104623.

Borgia, A., Delaney, P.T. & Denlinger, R.P., 2000. Spreading volcanoes, *Annu. Rev. Earth planet. Sci.,* **28,** 539–570.

Brooks, B.A., Foster, J.H., Bevis, M., Wolfe, C. & Behn, M., 2006. Periodic slow earthquakes on the flank of Kilauea volcano, Hawai'I, *Earth planet. Sci. Lett.,* **246,** 207–216.

Cervelli, P. & Miklius, A., 2003. The shallow magmatic system of Kilauea Volcano, *U.S. Geol. Surv. Prof. Pap.,* **1676,** 149–163.

Chen, C.W. & Zebker, H., 2000. Network approaches to two-dimensional phase unwrapping: intractability and two new algorithms, *J. Opt. Soc. Am.,* **17,** 401–414.

Chen, K., Smith, J.D., Avouac, J.-P., Liu, Z., Song, Y.T. & Gualandi, A., 2019. Triggering of the Mw 7.2 Hawaii earthquake of 4 May 2018 by a dike intrusion, *Geophys. Res. Lett.,* **46,** 2503–2510.

Cocco, M. & Rice, J.R., 2002. Pore pressure and poroelasticity effects in Coulomb stress analysis of earthquake interactions, *J. geophys. Res.,* **107**(B2), doi:10.1029/2000JB000138.

Darwin, C., 1840. On the connexion of certain volcanic phenomena in South America; and on the formation of mountain chains and volcanos, as the effect of the same power by which continents are elevated. *Geol. Soc. [London] Trans.,* **2,** 601–632.

Delaney, P.T., Miklius, A., Arnadottir, T., Okamura, A. & Sako, M., 1993. Motions of Kilauea volcano during sustained eruption from the PuuOo and Kapaianaha vents, 1983–1991, *J. geophys. Res.,* **98,** 17801–17820.

Denlinger, R.P. & Morgan, J.K., 2014. Instability of Hawaiian volcanoes, chap. 4 of Poland, M.P., Takahashi, T.J., and Landowski, C.M., eds., Characteristics of Hawaiian volcanoes, *U.S. Geol. Surv. Prof. Pap.,* **1801,** 149–175.

Dieterich, J.H., 1988. Growth and persistence of Hawaiian volcanic rift zones, *J. geophys. Res.,* **93,** 4258–4270.

Dieterich, J., Cayol, V. & Okubo, P., 2000. The use of earthquake rate changes as a stress meter at Kilauea volcano, *Nature,* **408,** 457–460.

Dieterich, J., Cayol, V. & Okubo, P., 2003. Stress changes before and during the Pu'u 'Ō'ō-Kūpianaha eruption, *Prof. Pap.,* **1676,** 187–202.

Dvorak, J.J. *et al.*, 1986. Mechanical response of the south flank of Kilauea volcano, Hawaii, to intrusive events along the rift zones, *Tectonophysics,* **124,** 193–209.

Foster, J.H., Lowry, A.R. & Brooks, B.A., 2013. Fault frictional parameters and material properties revealed by slow slip events at Kilauea Volcano, Hawai'I, *Geophys. Res. Lett.,* **40**(23), 6059–6063.

Freed, A.M., 2005. Earthquake triggering by static, dynamic, and postseismic stress transfer, *Annu. Rev. Earth Planet. Sci.,* **33,** 335–368.

Goldstein, R.M. & Werner, C.L., 1998. Radar interferogram filtering for geophysical applications. *Geophys. Res. Lett.,* **25**(21), 4035–4038.

Heliker, C. & Mattox, T.N., 2003. The first two decades of the Pu'u 'Ō'ō–Kupaianaha eruption: Chronology and selected bibliography, in The Pu'u 'Ō'ō-Kupaianaha eruption of Kīlauea Volcano, Hawai'I, *U.S. Geol. Surv. Prof. Pap.,* **1676,** 1–27.

Hill, D.P., Pollitz, F. & Newhall, C., 2002. Earthquake-volcano interactions, *Phys. Today,* **55**(11), 41–47.

Hills, D.J., Morgan, J.K., Moore, G.F. & Leslie, S.C., 2013. Structural Variability along the Submarine South Flank of Kilauea Volcano, Hawai'i, from a Multichannel Seismic Reflection Survey, *Hawaiian Volcanoes: Deep Underwater Perspectives,* **128,** doi:10.1029/GM128p0105.

Larson, K.M., Poland, M. & Miklius, A., 2010. Volcano monitoring using GPS: Developing data analysis strategies based on the June 2007 Kīlauea Volcano intrusion and eruption, *J. geophys. Res.,* **115,** B07406.

Lay, T., Ye, L., Kanamori, H. & Satake, K., 2018. Constraining the dip of shallow, shallowly dipping thrust events using long-period Love wave radiation patterns: applications to the 25 October 2010 Mentawai, Indonesia, and 4 May 2018 Hawaii Island earthquakes, *Geophys. Res. Lett.,* **45,** 10342–10349.

Liu, C., Lay, T. & Xiong, X., 2018. Rupture in the 4 May 2018 MW 6.9 earthquake seaward of the Kilauea east rift zone fissure eruption in Hawaii, *Geophys. Res. Lett.,* **45**(18), 9508–9515.

Lundgren, P. *et al.*, 2013. Evolution of dike opening during the March 2011 Kamoamoa fissure eruption, Kı-lauea Volcano, Hawai`I, *J. geophys. Res.,* **118,** 897–914.

Manga, M. & Brodsky, E.E., 2006. Seismic triggering of eruptions in the far field: Volcanoes and geysers, *Annu. Rev. Earth Planet. Sci.,* **34,** 263–291.

McTigue, D.F., 1987. Elastic stress and deformation near a finite spherical magma body: resolution of the point source paradox. *J. geophys. Res.,* **92,** 12931–12940.

Montgomery-Brown, E.K., Sinnett, D.K., Poland, M., Segall, P., Orr, T., Zebker, H. & Miklius, A., 2010. Geodetic evidence for en echelon dike emplacement and concurrent slow slip during the June 2007 intrusion and eruption at Kīlauea volcano, Hawaii, *J. geophys. Res.,* **115,** B07405, doi:10.1029/2009JB006658.

Montgomery-Brown, E.K., Poland, M.P. & Miklius, A., 2015. Delicate balance of magmatic-tectonic interaction at Kilauea Volcano, Hawai'i, revealed from slow slip events, *Geophys. Monogr.,* **13,** 208, doi:10.1002/9781118872079.ch13.

Morgan, J.K., Moore, G.F., Hills, D.J. & Leslie, S., 2000. Overthrusting and sediment accretion along Kilauea's mobile south flank, Hawaii: evidence for volcanic spreading from marine seismic reflection data, *Geology,* **28,** 667–700.

Morgan, J.K., Moore, G.F. & Clague, D.A., 2003. Slope failure and volcanic spreading along the submarine south flank of Kilauea volcano, Hawaii, *J. geophys. Res.,* **108**(B9), 2415, doi:10.1029/2003JB002411.

Neal, C.A. *et al.*, 2018. The 2018 rift eruption and summit collapse of Kīlauea Volcano, *Science,* eaav7046, doi:10.1126/science.aav7046.

Okada, Y., 1992. Internal deformation due to shear and tensile faults in a half-space, *Bull. seism. Soc. Am.,* **82**(2), 1018–1040.

Olivier, G., Brenguier, F., Carey, R., Okubo, P. & Donaldson, C., 2019. Decrease in seismic velocity observed prior to the 2018 eruption of Kīlauea Volcano with ambient seismic noise interferometry, *Geophys. Res. Lett.,* **46**(7), 3734–3744.

Owen, S., Segall, P., Lisowski, M., Miklius, A., Denlinger, R. & Sako, M., 2000a. Rapid deformation of Kilauea Volcano: global positioning system measurements between 1990 and 1996, *J. geophys. Res.,* **105**(B8), 18983–18998.

Owen, S., Segall, P., Lisowski, M., Miklius, A., Murray, M., Bevis, M. & Foster, J., 2000b. January 30, 1997 eruptive event on Kilauea Volcano, Hawaii, as monitored by continuous GPS, *Geophys. Res. Lett.,* **27,** 2757–2760.

Owen, S.E. & Burgmann, R., 2006. An increment of volcano collapse: kinematics of the 1975 Kalapana, Hawaii, earthquake, *J. Volc. Geotherm. Res.,* **150,** 163–185.

Poland, M.P., Miklius, A. & Montgomery-Brown, E., 2014. Magma supply, storage, and transport at shield-stage Hawaiian volcanoes, Chapter 5 of Poland, M. P., T. J. Takahashi, and C. M. Landowski, eds., Characteristics of Hawaiian Volcanoes, *U.S. Geol. Surv. Prof. Pap.,* **1801,** 179–234.

Poland, M.P., Peltier, A., Bonaforte, A. & Puglisi, G., 2017. The spectrum of persistent volcanic flank instability: a review and proposed framework based on Kīlauea, Piton de la Fournaise, and Etna, *J. Volc. Geotherm. Res.,* **339,** 63–80.

Pritchard, M.E., Jay, J.A., Aron, F., Henderson, S.T. & Lara, L.E., 2013. Subsidence at southern Andes volcanoes induced by the 2010 Maule, Chile earthquake, *Nat. Geosci.,* **6,** 632–636.

Sandwell, D., Mellors, R., Tong, X., Wei, M. & Wessel, P., 2011. Open radar interferometry software for mapping surface deformation. *EOS, Trans. Am. Geophys. Un.,* **92**(28), 234–234.

Segall, P., Desmarais, E., Shelly, D., Miklius, A. & Cervelli, P., 2006. Earthquakes triggered by silent slip events on Kilauea Volcano, Hawaii, *Nature,* **442,** 71–74.

Segall, P., Llenos, A.L., Yun, S.-H., Bradley, A.M. & Syracuse, E.M., 2013. Time-dependent dike propagation from joint inversion of seismicity and deformation data, *J. geophys. Res.,* **118,** 5785–5804.

Selva, J., Marzocchi, W., Zencher, F., Casarotti, E., Piersanti, A. & Boschi, E., 2004. A forward test for interaction between remote earthquakes and volcanic eruptions: the case of Sumatra (June 2000) and Denali (November 2002) earthquakes, *Earth planet. Sci. Lett.,* **226,** 383–395.

Takada, Y. & Fukushima, Y., 2013. Volcanic subsidence triggered by the 2011 Tohoku earthquake in Japan, *Nat. Geosci.,* **6,** 637–641.

Walter, T.R., Acocella, V., Neri, M. & Amelung, F., 2005. Feedback processes between magmatic events and flank movement at Mount Etna (Italy) during the 2002–2003 eruption, *J. geophys. Res.,* **110**(B10), B10205, doi:10.1029/2005JB003688.

Walter, T.R. & Amelung, F., 2006. Volcano-earthquake interaction at Mauna Loa volcano, Hawaii, *J. geophys. Res.,* **111**(B5), B05204, doi:10.1029/2005JB003861.

Walter, T.R. & Amelung, F., 2007. Volcanic eruptions following M $\geq$ 9 megathrust earthquakes: Implications for the Sumatra-Andaman volcanoes, *Geology,* **35,** 539–542.

Wang, L., Wang, R., Roth, F., Enescu, B., Hainzl, S. & Ergintav, S., 2009. After-slip and viscoelastic relaxation following the 1999 M7.4 Ízmit earthquake, from GPS measurements, *Geophys. J. Int.,* **178**(3), 1220–1237.

Wang, K. & Fialko, Y., 2015. Slip model of the 2015 Mw 7.8 Gorkha (Nepal) earthquake from inversions of ALOS-2 and GPS data, *Geophys. Res. Lett.,* **42**(18), 7452–7458.

Wang, K., Xu, X. & Fialko, Y., 2017. Improving burst alignment in TOPS interferometry with bivariate enhanced spectral diversity. *IEEE Geosci. Remote Sens. Lett.,* **14**(12), 2423–2427.

Wang, K. *et al.*, 2019. Interseismic quiescence and triggered slip of active normal faults of Kīlauea Volcano's South Flank during 2001–2018. *J. geophys. Res.,* **124**(9), 9780–9794.

Xu, X., Sandwell, D.T., Tymofyeyeva, E., Gonzalez-Ortega, A. & Tong, X., 2017. Tectonic and anthropogenic deformation at the Cerro Prieto geothermal step-over revealed by Sentinel-1A InSAR. *IEEE Trans. Geosci. Remote Sens.,* **55**(9), 1–9.

Yang, X.-M., Davis, P.M. & Dieterich, J.H., 1988. Deformation from inflation of a dipping finite prolate spheroid in an elastic half-space as a model for volcanic stressing, *J. geophys. Res.,* **93,** 4249–4257.

SUPPORTING INFORMATION

Supplementary data are available at *GJI* online.

Table S1. Source parameters derived by combining Spherical magma reservoir induced deformation and Okada (1992) dislocation model.

Figure S1. Variation of roughness (in bars) with the relative misfit between the observed and calculated coseismic offsets for varying smoothing parameter values. An optimal smoothing parameter of 0.2 is used to derive the coseismic rupture slip model.

Figure S2. The trade-off curve between the roughness (in bars) and the relative misfit in the observed and calculated average displacement rate during 2013–2018. An optimal value 0.2 of the smoothing parameter is applied to derive the pre-intrusion slip model.

Figure S3. Coseismic slip model of (a) horizontal and (b) vertical displacements obtained from Liu *et al.* (2018) by inversion of teleseismic body waves, strong-ground motion recordings, and coseismic GPS offsets along the southeastern coast of Hawaii. The RMS misfits of the slip model is 4.8 cm.

Figure S4. Parameters considered for modelling the surface deformation due to an expanding magma chamber beneath the Kīlauea summit caldera region. The solution depends on four parameters including the dimensionless pressure change $\Delta P/\mu$, and the source location in 3-D Cartesian coordinates (x_0, y_0, z_0). Lower panels represents the best-fitting model parameters, for which the misfit between the observed and model slip is minimum. The estimated volume for the volcanic eruption is found to be 9.22E + 06 m^3 yr^{-1}, at a depth of 5 km.

Figure S5. Parameters considered modelling the surface deformation due to an expanding magma chamber beneath the Mauna Loa region. The solution depends on four parameters including the dimensionless pressure change $\Delta P/\mu$, and the source location (x_0, y_0, z_0). The estimated volume for the volcanic eruption is found to be 4.76E + 06 m^3 yr^{-1}, at a depth of 5 km.

Figure S6. Average horizontal velocities (black arrows) during (a) 2013–2018 period preceding the 2018 dyke intrusion and faulting episode with respect to the site PMAU and (b) 1990–1996 period of south flank deformation with respect to site HP7_ from Owen *et al.* (2000a). The Kilauea and Mauna Loa summit reservoirs are marked by yellow circles and the *M* 6.9 epicentre is indicated by star. Note that radial displacements are observed only during the period of 2013–2018.

Figure S7. Observed, modelled and residual: ERZ dyke model derived from the inversion of pre-earthquake InSAR interferogram (04/20/2018–05/02/2018).

Please note: Oxford University Press is not responsible for the content or functionality of any supporting materials supplied by the authors. Any queries (other than missing material) should be directed to the corresponding author for the paper.